Journal of Aerosol Science 104 (2017) 66–78

Contents lists available at ScienceDirect

Journal of Aerosol Science

journal homepage: www.elsevier.com/locate/jaerosci

Characterization of an aerosol microconcentrator for analysis using microscale optical spectroscopies☆

Lina Zheng[a,b], Pramod Kulkarni[a,*], Konstantinos Zavvos[a,b], Huayan Liang[a,c], M. Eileen Birch[a], Dionysios D. Dionysiou[b]

[a] Centers for Disease Control and Prevention, National Institute for Occupational Safety and Health, Cincinnati, OH, USA
[b] Environmental Engineering and Science Program, Department of Biomedical, Chemical and Environmental Engineering, University of Cincinnati, Cincinnati, OH, USA
[c] Department of Mechanical and Materials Engineering, University of Cincinnati, Cincinnati, OH, USA

ARTICLE INFO

Keywords:
Microconcentration
Optical spectroscopy
Measurement sensitivity
Portable analytical instrumentation

ABSTRACT

Efficient microconcentration of aerosols to a substrate is essential for effectively coupling the collected particles to microscale optical spectroscopies such as laser-induced or spark microplasma, or micro-Raman or infrared spectroscopies. In this study, we present detailed characterization of a corona-based aerosol microconcentration technique developed previously (Diwakar & Kulkarni, 2012). The method involves two coaxial electrodes separated by a few millimeters, one held at a high electrical potential and the other grounded. The particles are collected on the collection (i.e., ground) electrode from a coaxial aerosol flow in a one-step charge-and-collect scheme using corona discharge and electrical precipitation between the two electrodes. Performance of the corona microconcentration method was determined experimentally by measuring collection efficiency, wall losses, and particle deposition density. An intrinsic spectroscopic sensitivity was experimentally determined for the aerosol microconcentrator. Using this sensitivity, we show that corona-based microconcentration is much superior to alternative methods, including filtration, focused impaction using aerodynamic lens, and spot collection using condensational growth. The method offers unique advantages for compact, hand-held aerosol analytical instrumentation.

1. Introduction

Concentrated collection of aerosols has been a topic of great interest in aerosol science. Microscopic concentration, i.e. collection of aerosol particles over a miniscule area (on the order of 1 mm^2 or less) at high number or mass density is particularly important for aerosol characterization using laser spectrometric methods, such as laser-induced breakdown, micro-Raman, and infrared spectroscopies that probe miniscule amounts of particulate samples (Diwakar, Kulkarni, & Birch, 2012; Diwakar & Kulkarni, 2012, Zheng, Kulkarni, Birch, Deye, & Dionysiou, 2016).

Depending on the application, concentration of aerosols, either to a substrate or in a suspended state, has been used to achieve different objectives, which range from increasing the number density of suspended particles, increasing the surface density of particles collected on a substrate, and increasing temporal rate of collection. Methods based on collection of aerosols on particulate

☆ Disclaimer—The findings and conclusions in this report are those of the authors and do not necessarily represent the views of the National Institute for Occupational Safety and Health. Mention of product or company name does not constitute endorsement by the Centers for Disease Control and Prevention.

* Corresponding author.
E-mail address: PSKulkarni@cdc.gov (P. Kulkarni).

http://dx.doi.org/10.1016/j.jaerosci.2016.11.007
Received 10 August 2016; Received in revised form 7 November 2016; Accepted 11 November 2016
Available online 17 November 2016
0021-8502/ Published by Elsevier Ltd.

filters, to obtain a time-integrated concentration, have been extensively used for routine aerosol monitoring (Raynor, Leith, Lee, & Mukund, 2011; Spurny, 1999). Methods based on spatial concentration of aerosols, for instance, by creating a focused particle beam, have been well studied and widely used for aerosol analysis by mass spectrometry (Liu, Ziemann, Kittelson, & McMurry, 1995; Ziemann, Liu, Rao, Kittelson, & McMurry, 1995). A virtual impactor has been used to increase the number density (per unit volume) of larger particles in the suspended state (Barr, Hoover, Kanapilly, Yeh, & Rothenberg, 1983), mainly for improvement of instrument detection sensitivity (Keskinen, Janka, & Lehtimäki, 1987; Wu, Cooper, & Miller, 1989) and for epidemiological and toxicological studies (Ghio, Kim, & Devlin, 2000; Sioutas, Koutrakis, & Burton, 1995). A condensational growth technique has also been employed for growing ultrafine particles to super-micron droplets under saturation conditions for subsequent spot collection on an impaction plate (Eiguren Fernandez, Lewis, & Hering, 2014; Hering, Spielman, & Lewis, 2014) or concentration in a virtual impactor (Sioutas, Kim, & Chang, 1999). Focused particle beams also have been employed for efficient collection over microscopic areas. These techniques achieve focusing by expanding the aerosol flow into a low pressure chamber, either through capillary (Murphy & Sears, 1964), converging nozzles (Dahneke & Flachsbart, 1972) or aerodynamic lenses (Liu et al., 1995). Such focused particle beam techniques have been applied to various measurements in aerosol systems. Aerodynamic lenses have been used as aerosol inlets in aerosol mass spectrometers for online single particle analysis (Lee, Cho, & Lee, 2008; Su, Sipin, Furutani, & Prather, 2004), and for aerosol analysis using laser-induced breakdown spectroscopy (Park, Cho, & Kwak, 2009). Most of the aerosol concentrating techniques discussed above require relatively large pumping capacity and bulky hardware and therefore are not suitable for portable and compact instrumentation. Electrostatic collection offers an alternative sampling method that enables use of high flow rates with minimal pressure drop and is suitable for compact field instrumentation. The point-to-plane type of electrostatic precipitator (ESP) allows one-step charging and collection of particles (Hinds, 1999). Several point-to-plane ESP particle samplers have been designed and evaluated (Cheng, Yeh, & Kanapilly, 1981; Miller, Frey, King, & Sunderman, 2010; Morrow & Mercer, 1964). Electrostatic collection has been mainly used for collecting samples for microscopic analysis (Fierz, Kaegi, & Burtscher, 2007; Miller et al., 2010).

Recently our group has developed a corona-based aerosol microconcentration method for efficient coupling with laser or spark emission spectroscopy (Diwakar et al., 2012; Diwakar & Kulkarni, 2012, Zheng et al., 2016). The previous studies mainly dealt with the characterization of analytical aspects of aerosol elemental measurements. In this study, we present detailed characterization and optimization of the same corona-based aerosol collection method, with a particular focus on evaluating its microconcentration efficiency vis-à-vis current aerosol focusing and spot collection methods. We use spark emission spectrometry as an analytical tool to probe the efficacy of aerosol microconcentration, and believe that this method can be effectively coupled with other optical spectroscopies such as Raman and infrared methods. Performance of this microconcentration method was evaluated experimentally by measuring collection efficiency, wall losses, and particle deposition density, and compared with those of the other microconcentration methods such aerodynamic focusing and spot collection using condensational growth.

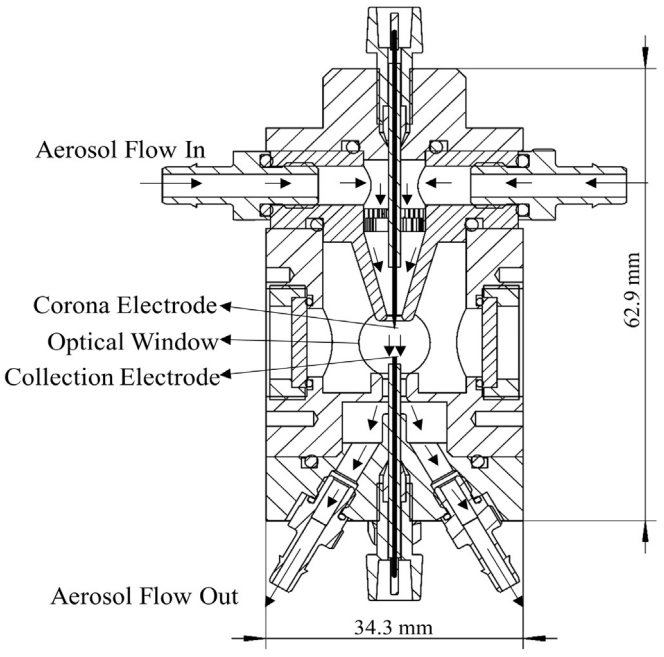

Fig. 1. Cross-section view of the corona aerosol microconcentrator.

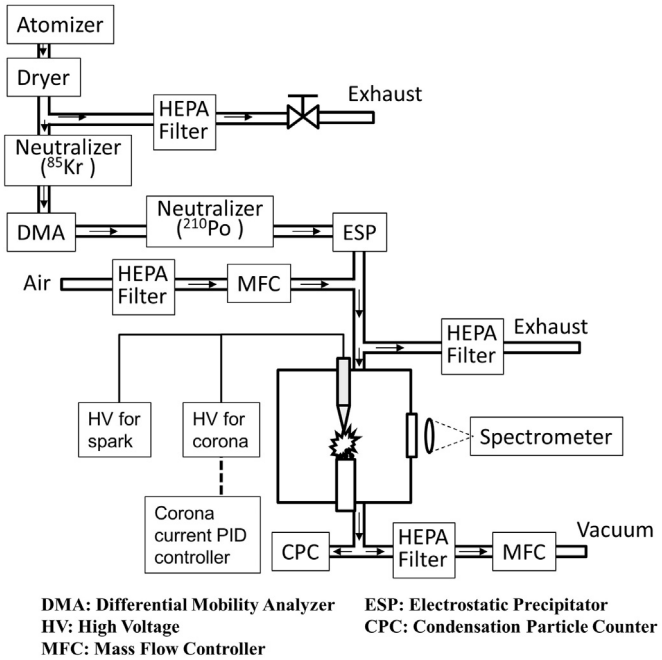

Fig. 2. Schematic diagram of experimental setup in this study.

2. Methods

2.1. Design of aerosol microconcentrator

Fig. 1 shows the schematic diagram of the corona aerosol microconcentrator (CAM) used in this study. The design of the CAM is similar to the aerosol collection systems used in earlier work in our group (Diwakar et al., 2012; Diwakar & Kulkarni, 2012; Zheng et al., 2016). The key components of the CAM include two coaxial electrodes with their tips separated by a distance of 5 mm. Both, the corona and collection (i.e., ground) electrodes, are made of tungsten. The corona electrode has a shaft diameter of 200 μm and converges to a sharp tip of radius 50 μm. The coaxial collection electrode has a relatively flat tip to provide a planar surface for particle deposition. Collection electrodes with four different diameters were investigated in this study: 500, 750, 1000, and 1500 μm. A high positive electric potential (4 – 6.2 kV) was applied on the corona electrode using a DC power supply (Bertan S-230, Spellman Corp., Hauppauge, NY, USA), whose output voltage was controlled using a PID controller to maintain a stable corona current between the corona and collection electrode. The side walls of the collection electrodes are covered with a dielectric sleeve made of polyether ether ketone (PEEK) (wall thickness varied depending on the electrode size; McMaster-Carr, Princeton, NJ, USA). The external dimensions of the CAM are approximately 3.4 × 3.4 × 6.3 cm. Optical access for optical signal collection is provided by UV-VIS coated fused silica windows on the CAM walls.

2.2. Experimental setup

The experimental setup, shown in Fig. 2, was designed to evaluate collection efficiency of the CAM and detection sensitivity of spark emission spectroscopy. Test aerosols were generated using an atomizer (model 3076, TSI Inc., Shoreview, MN, USA) to aerosolize $(NH_4)_2SO_4$ and $Cr(NO_3)_3$ solutions. The aerosol was subsequently dried in a diffusion dryer and then passed through a differential mobility analyzer (DMA; model 3081, TSI Inc., Shoreview, MN, USA), a ^{210}Po neutralizer, followed by an electrostatic precipitator (ESP) to remove all charged particles and obtain a near-monodisperse, uncharged test aerosol. The aerosol flow rate through the DMA was maintained at 0.23 L min^{-1}, and the sheath flow rate in DMA was 2.3 L min^{-1}. The aerosol exiting the ESP was diluted with HEPA-filtered air at a flow rate of 5 L min^{-1}. The aerosol flow through the CAM was driven by the native pump in the condensation particle counter (CPC; model 3022 A, TSI Inc., Shoreview, MN, USA) and a mass flow controller (MFC; model 247 C, MKS Instruments, Inc., Andover, MA, USA). The MFC was used to adjust the aerosol flow rate through the CAM chamber in a range of 0.6 – 5 L min^{-1}.

The particulate mass accumulated on the collection electrode tip of the CAM was measured using spark emission spectroscopy (SES) (Diwakar & Kulkarni, 2012; Zheng et al., 2016). In the SES system, a high voltage pulse generator (model ARC2-03C-R80A, Cascodium Inc., Andover, MA, USA) was used to produce a spark microplasma in the electrode gap to ablate the collected particulate matter from the collection electrode. The atomic emission signals from the spark microplasma were collected using an optical fiber connected to a spectrograph (IsoPlane SCT320, Princeton Instrument Inc., Trenton, NJ, USA) coupled with a gated ICCD camera (iStar 334 T, Andor Technology, South Windsor, CT, USA). A delay time of 5 μs and a gate width of 25 μs were used for spectral

acquisition. The atomic emission signal intensity measured during the spark discharge is directly proportional to the abundance of the analyte in the particulate mass deposited on the electrode tip. DMA classified monodisperse $Cr(NO_3)_3$ aerosol with a particle size of 100 nm in diameter was used for studies aimed at establishing collection characteristics of the CAM (with Cr as a target analyte in SES measurement). $(NH_4)_2SO_4$ test aerosol was used in experiments designed to measure particle loss on the electrode side walls.

2.3. Analysis of $(NH_4)_2SO_4$ aerosol

Ion chromatography (IC) analysis was used to measure the particulate mass of $(NH_4)_2SO_4$ deposited on the electrode. Concentration of the airborne $(NH_4)_2SO_4$ aerosol was determined by collecting aerosol on the polytetrafluoroethylene (PTFE) filter, followed by IC analysis. The extraction of $(NH_4)_2SO_4$ particles (collected on the electrode or filter) was done using the procedures described by Chow and Watson (1999). The collection substrate (electrode or the filter) was placed in an extraction vial and 200 μL of ethanol was added as wetting solution and 3 ml ultrapure DI water was added as a solvent. The vial was then sonicated for 15 minutes in an ultrasonic bath (Model ME 4.6, Mettler Electronics Corp., Anaheim, CA), followed by aging for 24 hours at 3 °C. This assured complete extraction of the deposited $(NH_4)_2SO_4$ particles in the solvent. The extracted solution in the vial was analyzed using IC (Dionex™, Thermo Fisher Scientific Inc., Sunnyvale, CA) for quantitative determination of sulfate ions. The calibration curve for SO_4^{2-} was constructed using five standard solutions with different concentrations in the range 0.01 – 2 mg L^{-1}.

3. Results and discussions

During the operation of the CAM, a high voltage is applied to the corona electrode to form a nonuniform electrostatic field between the corona electrode and the flat tip of the collection electrode. In the region of sufficiently high electric field strength at the tip of the corona electrode, air undergoes ionization and partial breakdown. Unipolar ions are continuously produced in the corona discharge process surrounding the tip of the corona electrode, which are then transported to the interelectrode space (Chang, Lawless, & Yamamoto, 1991). The incoming particles acquire electrical charge via diffusion and field charging mechanisms.

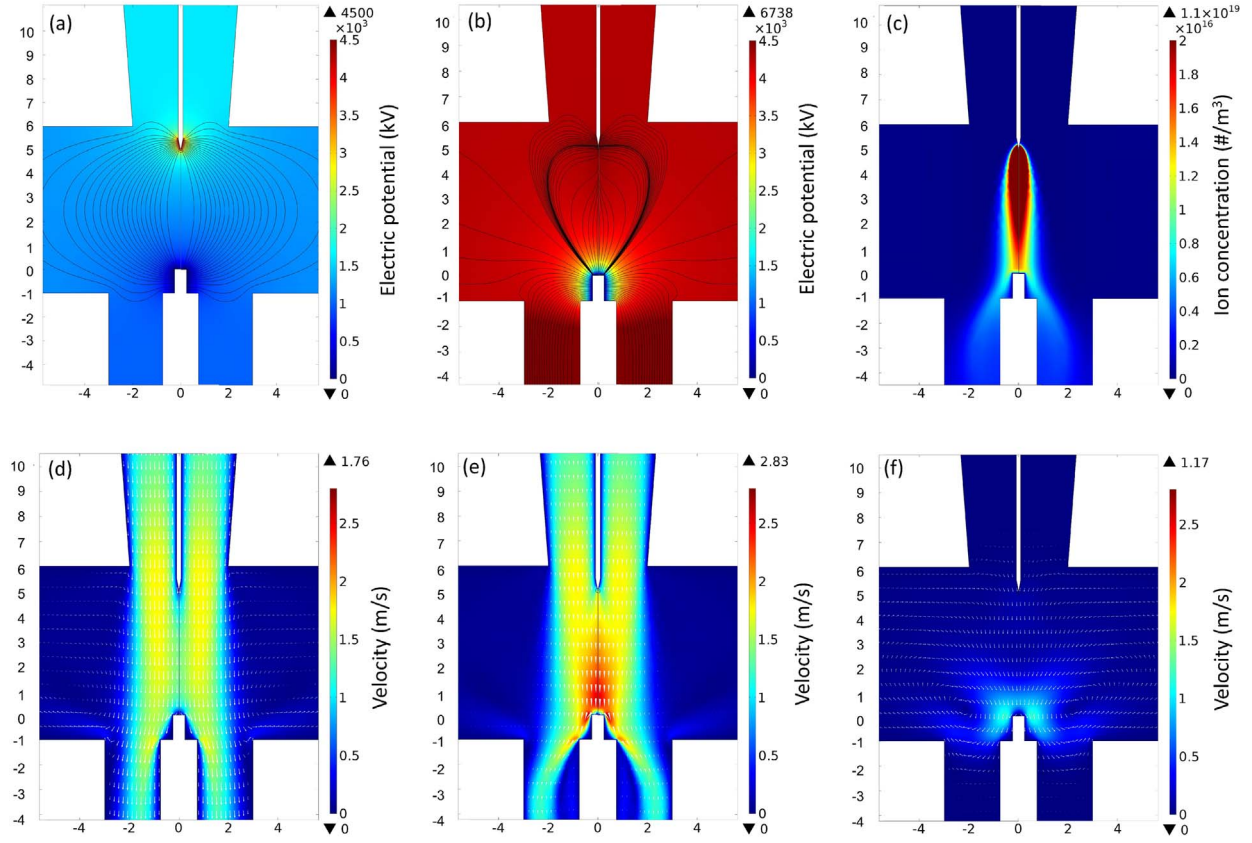

Fig. 3. Numerical simulation results: (a) distribution of electric potential in the absence of corona, (b) distribution of electric potential in the presence of corona, (c) distribution of ion concentration in the presence of corona, (d) flow velocity field in the absence of corona, (e) flow velocity field in the presence of corona, and (f) flow velocity field at 0 L min^{-1} in the presence of corona. X- and Y-axes show distance in millimeters. Electric field streamlines are also shown in (a) and (b). The arrows in (d), (e) and (f) indicate direction of flow velocity. The high voltage applied on the corona electrode was 4.5 kV and the volumetric flow rate through the CAM was 1 L min^{-1} in all numerical simulations [except in figure (f)]. The corona and collection electrodes were 200 μm and 500 μm in diameter, respectively. The interelectrode distance was 5 mm.

Subsequently, the charged particles migrate in the electric field and deposit on the collection electrode.

3.1. Simulation of particle transport and deposition

Numerical simulations were conducted to simulate particle charging and transport in the CAM. The distributions of electric potential, electric field, space charge density and velocity field around the corona and collection electrodes, with and without considering corona, were obtained using COMSOL™ Multiphysics software (COMSOL, Inc., Burlington, MA, USA). The details of the simulation approach are presented elsewhere (Liang, Kulkarni, Zheng, & Jog, 2015).

Fig. 3 shows the simulations results. In the absence of the corona, the contour plot of the electric potential in the CAM (Fig. 3(a)) shows the highest electric potential surrounding the tip of the corona electrode. However, in the presence of the corona, the potential distribution (Fig. 3(b)) is significantly different due to the space charge effect (Fig. 3(c)). Though the ion concentration is the highest in the interelectrode gap, there is still significant ion concentration in other regions of the CAM, away from the coaxial electrodes. Fig. 3(d) and (e) show the distribution of flow velocity in the presence and absence of corona. In the interelectrode gap, the flow velocities are about 1.3 m s^{-1} near the collection electrode in the absence of the corona and increase to 2.5 m s^{-1} in the presence of corona. Corona leads to higher flow velocities directed towards the collection electrode, which helps improve particle deposition. The higher flow velocity is attributed to the electrohydrodynamic (EHD) flow, which is caused by the momentum exchange between high-velocity ions migrating in the interelectrode space and the neutral gas species in the surrounding air (Robinson, 1961; Yabe, Mori, & Hijikata, 1978). This electrodynamic flow assists the migration of charged aerosol particles towards the collection electrode. The nature of EHD flow is evident in Fig. 3(f), which shows the distribution of the secondary flow entirely induced by the momentum transfer from migrating charged species to the neutral gas molecules. The corona discharge creates a rotational flow near the collection electrode, which helps with re-entrainment and focusing of the aerosol particles to the central region of the flow channel. The highest flow velocity of the swirl flow, directed towards the collection electrode, was found to be 1.17 m s^{-1}.

3.2. Collection efficiency of the CAM

The collection efficiency of the CAM is governed by the particle diameter, corona current, flow characteristics, electrode diameter, interelectrode distance, and the electrostatic field distribution. It is necessary to choose an optimum set of parameters to maximize the collection efficiency. Count-based particle collection efficiency (η_c) was estimated by measuring the particle number concentration downstream of the CAM using a CPC, with and without the presence of the electric field across the electrodes (N_{out}^{HV} and $N_{out}^{V=0}$).

$$\eta_c = (N_{out}^{V=0} - N_{out}^{HV})/N_{out}^{V=0} \quad (1)$$

Fig. 4 shows the collection efficiency for different electrode sizes (500 μm, 750 μm, 1000 μm, and 1500 μm in diameter, respectively) plotted as functions of the corona current at a flow rate of 1.5 L min^{-1}. As the corona current increases from 0.5 to 6 μA, the collection efficiency for relatively larger electrodes with diameters of 1000 μm and 1500 μm increases approximately by 25%. These trends are consistent with a study reported earlier (Miller et al., 2010) on a hand-held electrostatic precipitator, with a collection electrode 3 mm diameter. Higher voltage leads to higher corona current and higher charging efficiency, leading to higher collection efficiency. For the smaller electrodes (500 and 750 μm diameter), however, the collection efficiency does not vary much with corona current. Fig. S-1 in the Supplemental Information (SI) shows voltage-current characteristics of the CAM for different sizes of collection electrodes. A maximum high voltage exists for mantaining a stable corona current, and higher voltage beyond the maximum leads to frequent sparking or instability. A stable corona current of 5 μA was used for all the subsequent experiments in

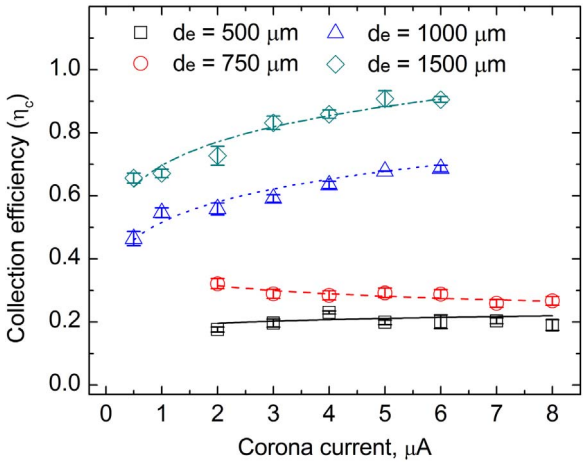

Fig. 4. Collection efficiency as a function of corona current at a volumetric flow rate of 1.5 L min^{-1} for different collection electrodes. Distance between the corona and the collection electrode was 5 mm. The particle size was 100 nm in diameter. The lines represent the best fit to the experimental data.

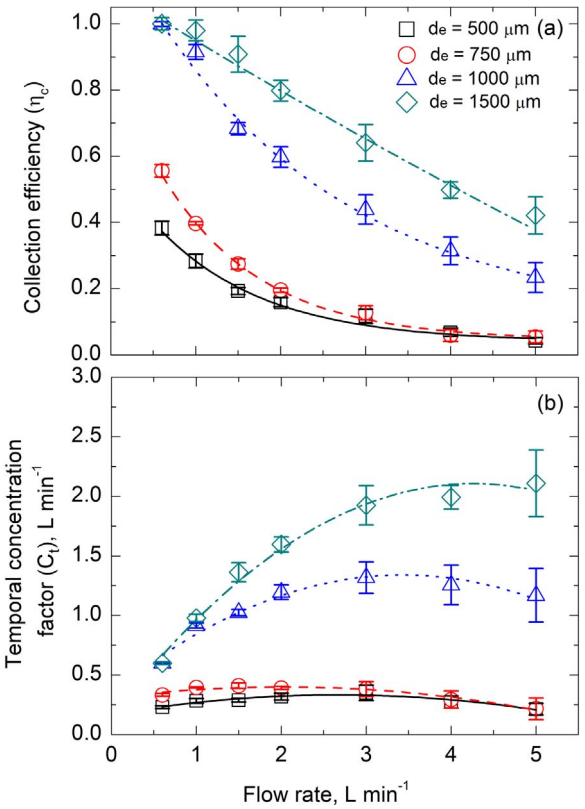

Fig. 5. Variation of (a) collection efficiency, and (b) temporal concentration factor as a function of aerosol flow rate for various electrode diameters. The corona current was 5 μA. The particle size was 100 mm in diameter. The error bars represent standard deviation calculated from three replicate measurements. The lines represent best fits to the experimental data.

this study. Fig. 4 also shows that a larger collection electrode provides a higher collection efficiency, due to a larger deposition surface and a higher electric field strength from a higher voltage under the same corona current (as shown in Fig. S-1 in SI).

Fig. 5(a) shows the collection efficiency plotted as a function of aerosol flow rate for various electrode diameters. As the flow rate increases from 0.6 to 5 L min^{-1}, the collection efficiency decreases for all four electrodes. However, to maximize the sensitivity of the system, it is the total particulate mass collected on the electrode tip that must be maximized. This collected mass is directly proportional to the flow rate (Q) and the collection efficiency (η). Fig. 5(b) shows the plot of product $\eta \times Q$ as a function of flow rate. This product signifies the time-rate of microconcentration, and will be denoted as the temporal concentration factor (C_t) in this study. The variation of C_t with Q for a given collection electrode are described using parabolic best fit curves and are shown in

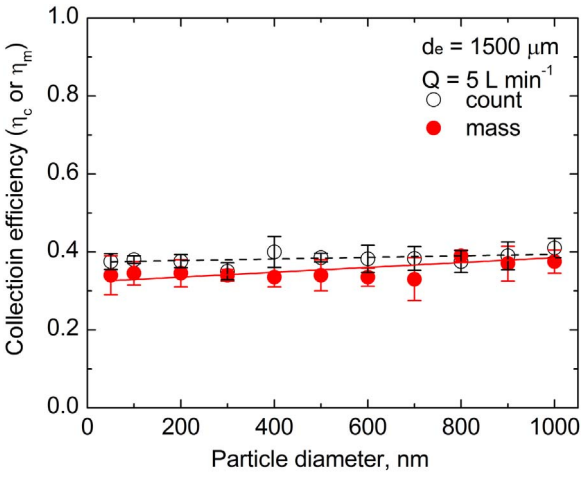

Fig. 6. Comparison of collection efficiency obtained from counting particles by CPC and by determining mass by IC analysis. The corona current was 5 μA. The error bars represent standard deviation calculated from three replicate measurements. The lines represent best fits to the experimental data. (Zavvos, 2016).

Fig. 5(b). The figure shows that C_t is low at very low flow rates even though the collection efficiency is high, then increases with increasing flow rate and reaches a maximum. After the maximum, C_t starts decreasing with further increase of the flow rate because of the low collection efficiency. Maximum C_t can be achieved at a flow rate of approximately 3 L min^{-1} for 500, 750, and 1000 μm electrodes, and at 5 L min^{-1} for 1500 μm electrode. The figure also shows that the collection efficiency and the concentration factor also increase with the increasing collection electrode diameter at a given aerosol flow rate.

The collection efficiency presented in Fig. 5 was based on the measurement of aerosol number concentration at the outlet of the CAM in the presence and the absence of high voltage on the corona electrode (Eq. (1)). Alternatively, collection efficiency was also obtained using an independent method involving direct measurement of the accumulated mass of particles on the collection electrodes (Zavvos, 2016). In these experiments, the DMA classified $(NH_4)_2SO_4$ test aerosol was first collected on the collection electrode for a predetermined period of time at a given aerosol flow rate. Simultaneously, to determine the air concentration of the $(NH_4)_2SO_4$ aerosol entering the CAM, a filter sample was collected at the inlet of the CAM. The particulate mass deposited on the electrode ($m_{electrode}$) and that collected on the filter (m_{filter}), over a predetermined period of time, was analyzed for $(NH_4)_2SO_4$using IC analysis. The mass-based collection efficiency (η_m) was then calculated as,

$$\eta_m = m_{electrode}/m_{filter} \tag{2}$$

Fig. 6 shows the comparison of collection efficiencies obtained using both count- and mass-based measurement methods. Both these methods implicitly account for particle losses to walls. Measuring the number concentration at the 'outlet' implicitly accounts for the wall losses. In the mass-based method, the collection efficiency was determined by directly measuring particulate mass deposited on the electrode (tip and sidewall), which accounts for the wall losses. The difference in collection efficiency in Fig. 6 is small and is approximately within the range of experimental uncertainty of these measurements. Mean uncertainty was obtained using the linear best fit to the experimental data for both the methods. The mean count-based collection efficiency was approximately 2% greater than the mean mass-based collection efficiency in the particle diameter range 50–1000 nm. This demonstrates the equivalency of the two methods. The count-based method was used in the remainder of this study due to its ease of use.

3.3. Effects of particle size on collection efficiency

To measure airborne concentration of an analyte in an unknown polydisperse aerosol sample, a key requirement is that the collection efficiency is independent of the particle size. To examine the size dependence, the collection efficiency of the CAM was measured at different particle diameters in the submicrometer size range using the count-based method and the results are shown in Fig. 7. The figure shows a slight increase in collection efficiency as a function of particle size. For each case, a linear best fit to the experimental data is shown. For the 500 μm electrode at 1 L min^{-1}, the collection efficiency remains relatively constant, within the range of experimental uncertainty, over the submicrometer particle size range. When using the 500 μm electrode at 3 L min^{-1} and the 1000 μm electrode at 3 L min^{-1} and 5 L min^{-1}, the collection efficiency increases slightly with particle diameter. Similar results were obtained in early studies on collection efficiency of electrostatic precipitators. Cheng et al. (1981) showed that the collection efficiency of a point-to-plane electrostatic precipitator increases with increasing particle size at 0.1 – 1 L min^{-1}, and minimal effects of particle size on collection efficiency were found at the lowest flow rate (0.1 L min^{-1}) in their study. Laskin and Cowin (2002) also found a nearly constant collection efficiency for 0.1 – 1 μm particles using a point-to-plate electrostatic precipitator operated at a relatively low flow rate of 0.3 L min^{-1}. However, the collection efficiency of CAM was relatively independent of particle size even at a higher flow rate (1 L min^{-1}) using 500 μm collection electrode, and its increasing trend with particle diameter at 3 L min^{-1} was less significant than that reported by Cheng et al. (1981), which may be due to different orientation of flow and electric field configuration.

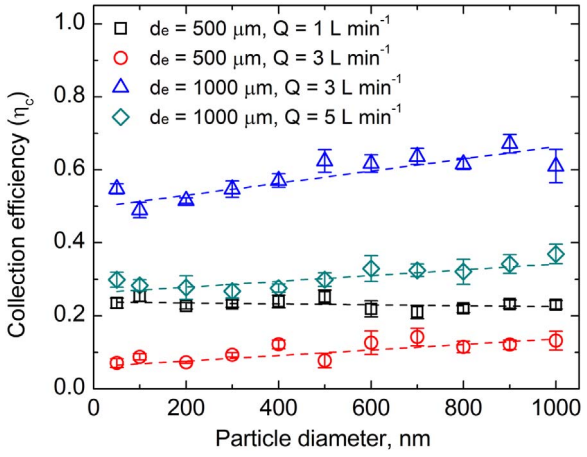

Fig. 7. Variation of collection efficiency as a function of particle size for different electrode diameters and flow rates at a corona current of 5 μA. The error bars represent standard deviation calculated from three replicate measurements. The lines represent best fits to the experimental data.

Although the collection efficiency exhibits a slight increasing trend with increasing particle diameter at 3 and 5 L min^{-1}, the size dependence of collection efficiency in Fig. 7 can be assumed to be represented by a mean value calculated over the entire size range. However, such an approximation may lead to a finite uncertainty, the degree of which will depend on the flow rate, electrode size, and the aerosol size distribution entering the CAM. For a 500 μm electrode, at 3 L min^{-1}, assuming a mean collection efficiency (~10.5%, which is the mean of the measured collection efficiency over the entire particle size range) leads to an error ranging from 0.06% to 36% depending on the nature of the lognormal distribution, as shown in Fig. S-2 in SI. For a typical urban aerosol in the accumulation mode which has a count median diameter (d_{pg}) of 100 nm and a geometric standard deviation (σ_g) of 1.8, the error is estimated to be about 13%.

3.4. Deposition uniformity and side wall losses

The variation of number density of particles deposited on the electrode surface was probed using scanning electron microscopy (SEM) (Zavvos, 2016). Fig. S-3 in SI shows SEM images of the collection electrode surface after colletion of particles on a 1500 μm electrode over 5, 10, and 20 minutes. Green fluorescent polystyrene latex (PSL) particles with a diameter of 2 μm were used as a test aerosol (using particles smaller than 2 μm could not be imaged reliably over a wider electrode area). The spatial distribution of particles was approximately homogeneous over the flat electrode surface.

During particle collection, due to favorable electrical field and flow conditions (Fig. 3), some particles can deposit on the electrode side walls (along its axis) instead of its flat tip. This particulate mass is not ablated by the microplasma. This unablated particulate mass needs to be accounted for to allow accurate retreival of airborne analyte concentration. Two methods were used to quantify the particle loss to the side walls of the electrode: i) counting the particles on side walls using SEM micrographs, and ii) extracting and analyzing the mass of $(NH_4)_2SO_4$ particles deposited on the side walls by IC chemical analysis (Zavvos, 2016). Fig. S-4(b) and Fig. S-4(c) in SI shows particle depostion on the flat tip as well as on the side walls. By counting individual particles per unit area of the micrograph, the fraction of particles deposited on the side walls was estimated to be 7.7%.

In the alternative method using IC analysis, $(NH_4)_2SO_4$ particles were collected on two electrodes in two separate experiments: a bare electrode and another identical electrode with a mask of thin Teflon™ layer wrapped around its side walls. The two electrodes are shown in Fig. S-5 in SI. The Teflon™ mask wrapped around the electrode side walls prevented the particles from depositing directly on the electrode walls. After each particle collection cycle, the total particulate mass deposited on the bare electrode (Fig. S-5(a)) and masked electrode (Fig. S-5(b)) was extracted in separate vials and analyzed for $(NH_4)_2SO_4$ using IC. Prior to the extraction step, the Teflon™ mask on the masked electrode was carefully removed. These measurements yielded the total analyte mass on the bare electrode (m_{total}; which included particles on the flat tip as well as side walls) and that deposited only on the flat tip (m_{tip}) from the masked electrode. The fraction of mass deposited on the side walls was calculated using the following equation:

$$\eta_{loss} = (m_{total} - m_{tip})/m_{total} \quad (3)$$

Fig. 8 shows the fraction of the particulate mass deposited on the side walls of the collection electrode. The particle loss was in the range of 8–17%, slightly higher than the crude estimate of 7.7% obtained from the SEM counting method. Based on these measurements, a constant factor of 12.8%, the mean of the particle loss over different particle diameters, was applied for retrieval of air concentrations to account for wall losses.

3.5. Effects of spark ablation on collection efficiency

The coaxial electrode system was used for particle collection as well as for generation of spark discharge in the interelectrode gap for atomic emission measurement. Each analyte measurement task entailed a cyclical sequence of two steps involving collection over

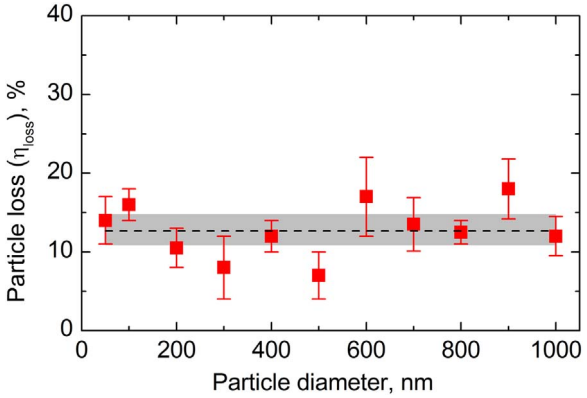

Fig. 8. The fraction of the particulate mass deposited on the side walls of the collection electrode. The two coaxial electrodes were made of tungsten. The error bars represent one standard deviation of three replicate measurements. The dash line represents the mean of collection efficiency over different number of sparks. The grey shaded band represents the 95% confidence interval. (Zavvos, 2016).

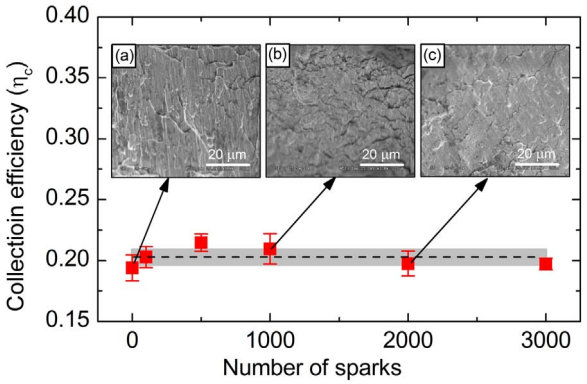

Fig. 9. Variation of collection efficiency as a function of number of sparks (100 nm particles and 1.5 L min^{-1}, 500 μm electrode, 5 μA current) and SEM images of collection electrode surface after (a) 0, (b) 1000, and (c) 2000 sparks. The error bars represent standard deviation calculated from three replicate measurements. The dash line represents the mean of collection efficiency over different number of sparks. The grey shaded region represents area within the 95% confidence interval.

a predetermined time period, followed by multiple ablation events (needed to record emission signal, and subsequently clean the collection surface for the next collection cycle). Depending on the electrode material, it is possible that the repeated spark discharges could alter the morphology of the collection electrode surface, which in turn, may influence the stability of corona or collection characteristics. Experiments were conducted to probe the effect of the number of spark discharges on the electrode collection efficiency. Fig. 9 shows the variation in particle collection efficiency of the CAM as a function of the number of spark discharges. A continuous train of pulsed spark discharges was produced at a frequency of 10 Hz and particle collection efficiency was experimentally measured (using the procedure described earlier; Eq. (1)) after every 100, 500, 1000, 2000, and 3000 spark discharges (using the same corona and collection electrodes). As shown in Fig. 9, the variation in collection efficiency was within 2% and no significant changes in the collection efficiency was observed even after 3000 sparks. Also shown (Fig. 9) are SEM images exhibiting the surface morphology of the collection electrode after 0, 1000, and 2000 sparks (Zavvos, 2016). No significant change in surface morphology of the electrodes (at the scale shown) were observed even after several thousand ablation events. It should be noted that the corona electrode or the anode does not exhibit any significant wear after several thousand spark discharge cycles, allowing reproducible corona operation and spark discharge measurements.

3.6. Analytical sensitivity

To examine the efficiency of microconcentration, collected particulate mass on the electrode surface was analyzed using spark discharge emission spectroscopy to determine the elemental concentration. Calibration curves were constructed by plotting emission signal intensity as a function of particulate mass. The slope of this calibration curve, denoted here as the mass-based sensitivity (S_m), is an important indicator of the efficacy of microconcentration as well as the overall analytical sensitivity of the method. Fig. 10(a) shows the calibration curves for Cr constructed for collection electrodes of various diameters (500, 750, 1000, and 1500 μm). DMA classified monodisperse $Cr(NO_3)_3$ particles with a diameter of 100 nm were used for calibration. As shown in Fig. 10(a), S_m increases with decreasing collection electrode diameter. This suggests efficient coupling of the concentrated particulate mass with the spark

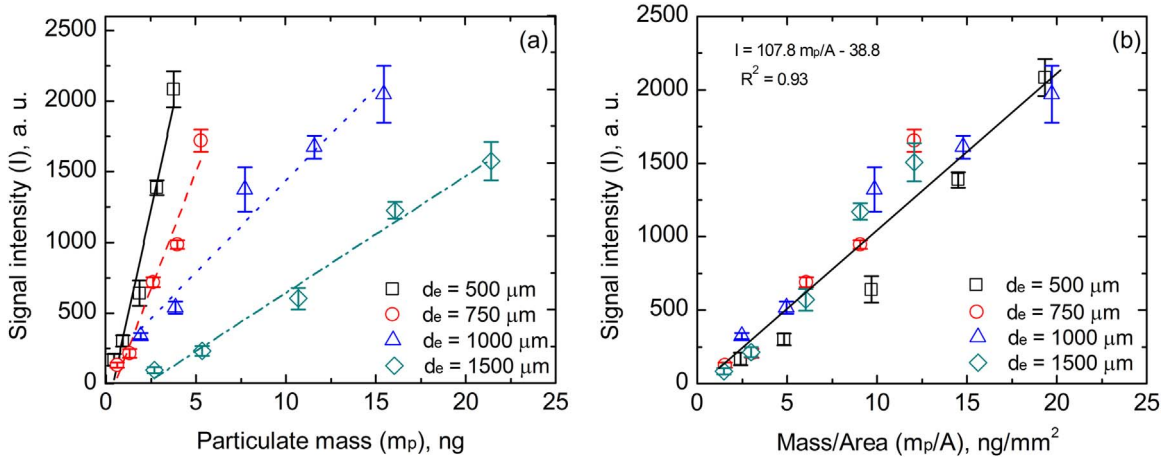

Fig. 10. (a) Calibration curves for Cr using different electrode diameters (Cr I 360.534 nm emission line was used in calibration); (b) The signal intensity of Cr from spark emission spectroscopy as a function of particulate mass (as Cr) per area. The lines represent linear fits to the experimental data.

microplasma for small diameter electrodes. The data in Fig. 10(a) can be collapsed into one curve when plotted as a function of surface mass density, defined as the particulate mass (as Cr) per unit area of the electrode surface. Fig. 10(b) shows signal intensity as a function of surface mass density ($\frac{m_p}{A}$),

$$I = S^* \frac{m_p}{A} \tag{4}$$

where I is the atomic emission signal intensity of the SES, S^* is the slope of the calibration curve in Fig. 10(b), m_p is the mass (as Cr) of particles collected on the electrode (ng), and A is the flat area of the collection electrode (mm^2). Here, we defined S^* as the intrinsic spectroscopic sensitivity of the CAM. For a specific spectroscopic system, S^* is a constant for a given analyte. In our system, S^* for Cr was measured to be 107.8 ng^{-1} mm^2. Eq. (4) implies that the signal intensity is a function of surface mass density on the electrode, rather than the absolute total mass itself. This could be explained by the fact that the fraction of the electrode surface sampled by the microplasma during ablation is limited by its finite spatial extent: this fraction is higher when the electrode diameter is equal to or smaller than the diameter of the ablation spot created by the microplasma on the electrode surface. To measure the diameter of the ablation spot, an aluminum disk (25 mm in diameter) was used as a cathode, and a PTFE filter (0.2 mm in thickness) was placed on the disk. After several spark discharges, the ablation area on the PTFE filter was measured using an optical microscope and found to be 510 ± 130 μm in diameter. This size of the ablation spot is comparable to diameter of 500 μm electrode, which was found to have the highest sensitivity in Fig. 10(a).

A larger diameter electrode provides higher particle flux (i.e. time rate of collection) to the electrode surface, therefore leads to a higher temporal concentration factor (C_t). On the other hand, a smaller diameter electrode offers better surface mass density or higher spatial concentration factor. Both the temporal and spatial aspects of microconcentration are important for achieving superior detection limits in terms of air concentration of the analyte. Using $m_p = \eta C_{in} Q t$ in Eq. (4), the emission signal intensity can be expressed as,

$$I = \frac{S^* \eta Q t}{A} C_{in} \tag{5}$$

where η is the collection efficiency; Q is the air flow rate (L min^{-1}), t is the particle collection time (min), and C_{in} is the incoming aerosol particle mass concentration (ng L^{-1}). The measurement sensitivity (S_c) of the analyte in terms of air concentration is then given by,

$$S_c = \frac{S^* \eta Q t}{A} \tag{6}$$

For most aerosol measurement applications, the objective is to maximize S_c. For our system, this requires an optimum combination of flow rate and electrode diameter. Fig. 11 shows the detection sensitivity (S_c) calculated using Eq. (6) at different flow rates and different electrode diameters for an assumed sampling time of 1 minute. The figure shows that S_c for most electrodes has a maximum; it first increases with increasing flow rate, and then decreases at higher flow rates (the maximum for 1500 μm electrode probably occurs beyond 5 L min^{-1} and was not measured experimentally). This trend is consistent with those in temporal concentration factor C_t in Fig. 5(b). Each electrode diameter has an optimum window of flow rate which provides the highest sensitivity. The highest sensitivity (193 μg^{-1} m^3 for Cr I) can be achieved at a flow rate of approximately 3 L min^{-1} for the 500 μm electrode. The error bars in Fig. 11 represent the standard deviation of three experimentally measured sensitivity (S_c), which is in the range of 0.6–35 μg^{-1} m^3; this uncertainty increases with flow rate. The detection sensitivity can be used to obtain limit of detection (LOD) for a given analyte. The LOD was estimated using 3-σ criteria defined by the International Union of Pure and Applied

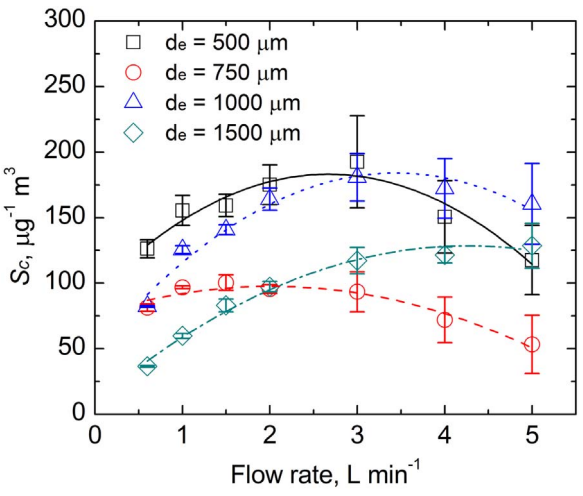

Fig. 11. Measurement sensitivity (S_c) of Cr I using CAM at different air flow rates and different electrode diameters. The error bars represent standard deviation. The lines represent best fits to the experimental data.

Chemistry (IUPAC) as,

$$LOD = 3\sigma/S_c \quad (7)$$

where σ is the standard deviation of the blank at the selected spectral region. The lowest LOD for Cr was estimated to be 0.1 μg m^{-3} using 500 μm electrode at 3 L min^{-1} with a sampling time of 1 minute. As a comparison, it is worth noting that the LOD of a filter-based method using inductively coupled plasma - atomic emission spectrometry (ICP-AES) is approximately 0.23 μg m^{-3} for an 8-hr sample (at 2 L min^{-1}) (NIOSH, 2003). The CAM used in this work offers a factor of 2 improvement in LOD at a sampling time that is over two orders of magnitude smaller. This demonstrates a clear advantage of microconcentration when coupling with microplasma spectroscopies.

The intrinsic spectroscopic sensitivity (S^*) for an analyte discussed earlier (Fig. 10(b)) is a characteristic constant for the specific electrode configuration and plasma characteristics used in our study. It must be noted that this intrinsic sensitivity (S^*) does not depend on the method employed to collect particles on the collection electrode. Therefore, S^* is independent of particle collection method. This allows probing and comparing the efficacy of alternative particle collection methods using filtration, aerodynamic lens, or inertial impaction. However, for the S^* to be applicable to other collection methods, it must be ensured that the spark discharge characteristics and the analyte ablation characteristics remain the same when the alternative collection methods are coupled with our spark emission spectroscopy method. This requirement should not be difficult to meet for most alternative particle collection methods. Using the characteristic S^* value for Cr I measured for the CAM, the sensitivities (i.e. S_c) one could achieve using alternative particle collection methods, including filtration, condensational growth followed by focused impaction, and focused impaction using aerodynamic lens, were calculated and compared with that of the CAM. Typical design and operating parameters such as collection efficiency, flow rate, particle deposition area, and sampling time for each collection method were assumed for each collection method and are shown in Table 1. Fig. 12 shows the calculated measurement sensitivity (S_c) obtained for alternative collection methods as a function of the aerosol sampling flow rate. The S_c for CAM (Fig. 12) is the experimentally measured data (except at 0.1 L min^{-1}, which was estimated by assuming 100% collection efficiency). The figure shows that the CAM used in this work provided the highest sensitivity, which varied from 41 to 193 μg^{-1} m^3 for Cr I for flow rates ranging from 0.1 to 5 L min^{-1}. The sensitivity for filter-based method was lower by 1 – 2 orders of magnitude, even when using large sampling flow rates. This again demonstrates the advantages of spatial microconcentration when coupling to microscale spectroscopies. At 0.1 L min^{-1}, S_c from aerodynamic lens is 54 μg^{-1} m^3, while that from CAM is 41 μg^{-1} m^3; however, 0.1 L min^{-1} is rather a large flow rate for aerodynamic lens and involves system operation at low pressure requiring very large pumping capacity. Sensitivity comparable to that of CAM can be achieved by the condensational growth droplet concentrator at relatively high flow rates; for example, S_c from the condensational growth method of 137 μg^{-1} m^3 (compared to 155 μg^{-1} m^3 for CAM) can be achieved at 1 L min^{-1}. However, higher flow rates in the condensational growth method requires relatively bulky hardware, making it unsuitable for compact hand-portable instrumentation.

4. Conclusions

A corona-based particle microconcentrator was characterized to evaluate its concentration efficacy using spark microplasma optical emission spectroscopy. The particle collection efficiency of the CAM was found to be relatively independent of particle size in the submicrometer diameter range under the operating conditions studied. The atomic emission signal was found to be a function of the surface density of the analyte. An intrinsic spectroscopic sensitivity of CAM for Cr was determined to be 107.8 ng^{-1} mm^2 (for the spark emission measurements). Using this intrinsic sensitivity, it was shown that the CAM offers the highest spectroscopic sensitivity compared to alternative particle collection methods such as filtration, focused impaction using aerodynamic lens, and spot collection using condensational growth (followed by impaction). Compared to widely-used filter-based atomic emission methods, the CAM offers drastic improvements in LOD and time resolution of analytical measurement in optical spectroscopies. Although, the efficacy of the microconcentration method was demonstrated using spark emission spectroscopy in this work, the method can be readily used for sensitive aerosol analysis using other microscale laser spectroscopies such as laser-induced breakdown, Raman, infrared, and UV-VIS spectroscopies. The method is particularly well-suited for compact, field-portable or personal instrumentation.

Table 1
Design and operating parameters of alternative particle collection methods for submicrometer size range.

Particle concentration methods	Collection efficiency (%)	Flow rate (L min^{-1})	Diameter of particle deposition area (mm)	Sampling time (minute)
Filtration	100	1–20	13[c]	1
Aerodynamic lens[a]	96–99	0.01–0.2	0.5	1
Condensational growth droplet concentrator	100	0.1–1	1	1
CAM[b]	4–100	0.1–5	0.5	1

[a] A design tool for aerodynamic lens system (Wang & McMurry, 2006a, 2006b) was used to obtain the design and performance parameters for 100 nm test particles.

[b] The collection efficiency of CAM at 0.6, 1, 1.5, 2, 3, 4, and 5 L min^{-1} was obtained experimentally, and the collection efficiency at 0.1 L min^{-1} was assumed to be 100%.

[c] 13 mm filter from SKC Inc., is assumed as a conservative estimate, though 25 mm and 37 mm filter are most common for personal sampling.

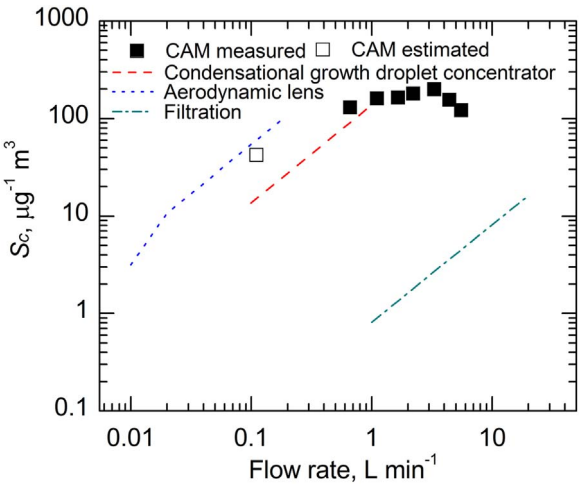

Fig. 12. Comparison of the measurement sensitivity (S_c) of CAM with alternative concentration or collection methods employing condensational growth droplet concentrator, aerodynamic lens, and filtration.

Acknowledgements

The authors would like to thank Joseph Fernback for SEM images. Authors would like to thank Dr. Chaolong Qi and Gregory Deye for helpful comments on the manuscript.

Appendix A. Supporting information

Supplementary data associated with this article can be found in the online version at doi:10.1016/j.jaerosci.2016.11.007.

References

Barr, E. B., Hoover, M. D., Kanapilly, G. M., Yeh, H. C., & Rothenberg, S. J. (1983). Aerosol concentrator design, construction, calibration, and use. *Aerosol Science and Technology*, 2(4), 437–442. http://dx.doi.org/10.1080/02786828308958647.

Chang, J. S., Lawless, P. A., & Yamamoto, T. (1991). Corona discharge processes. *IEEE Transactions on Plasma Science*, 19(6), 1152–1166.

Cheng, Y.-S., Yeh, H.-C., & Kanapilly, G. M. (1981). Collection efficiencies of a point-to-plane electrostatic precipitator. *The American Industrial Hygiene Association Journal*, 42(8), 605–610.

Chow, J. C., & Watson, J. G. (1999). Ion chromatography in elemental analysis of airborne particles. *Elemental Analysis of Airborne Particles*, 1, 97–137.

Dahneke, B., & Flachsbart, H. (1972). An aerosol beam spectrometer. *Journal of Aerosol Science*, 3(5), 345–349. http://dx.doi.org/10.1016/0021-8502(72)90089-4.

Diwakar, P., Kulkarni, P., & Birch, M. E. (2012). New approach for near-real-time measurement of elemental composition of aerosol using laser-induced breakdown spectroscopy. *Aerosol Science and Technology*, 46(3), 316–332. http://dx.doi.org/10.1080/02786826.2011.625059.

Diwakar, P. K., & Kulkarni, P. (2012). Measurement of elemental concentration of aerosols using spark emission spectroscopy. *Journal of Analytical Atomic Spectrometry*, 27(7), 1101–1109. http://dx.doi.org/10.1039/c2ja30025g.

Eiguren Fernandez, A., Lewis, G. S., & Hering, S. V. (2014). Design and laboratory evaluation of a sequential spot sampler for time-resolved measurement of airborne particle composition. *Aerosol Science and Technology*, 48(6), 655–663. http://dx.doi.org/10.1080/02786826.2014.911409.

Fierz, M., Kaegi, R., & Burtscher, H. (2007). Theoretical and experimental evaluation of a portable electrostatic TEM sampler. *Aerosol Science and Technology*, 41(5), 520–528.

Ghio, A. J., Kim, C., & Devlin, R. B. (2000). Concentrated ambient air particles induce mild pulmonary inflammation in healthy human volunteers. *American Journal of Respiratory and Critical Care Medicine*, 162(3), 981–988.

Hering, S. V., Spielman, S. R., & Lewis, G. S. (2014). Moderated, water-based, condensational particle growth in a laminar flow. *Aerosol Science and Technology*, 48(4), 401–408. http://dx.doi.org/10.1080/02786826.2014.881460.

Hinds, W. C. (1999). *Aerosol technology: properties. behavior, and measurement of airborne particles* (2nd edition) New York, NY: John Willey Sons, Inc..

Keskinen, J., Janka, K., & Lehtimäki, M. (1987). Virtual impactor as an accessory to optical particle counters. *Aerosol Science and Technology*, 6(1), 79–83.

Laskin, A., & Cowin, J. P. (2002). On deposition efficiency of point-to-plate electrostatic precipitator. *Journal of Aerosol Science*, 33(3), 405–409.

Lee, K.-S., Cho, S.-W., & Lee, D. (2008). Development and experimental evaluation of aerodynamic lens as an aerosol inlet of single particle mass spectrometry. *Journal of Aerosol Science*, 39(4), 287–304. http://dx.doi.org/10.1016/j.jaerosci.2007.10.011.

Liang, H., Kulkarni, P., Zheng, L., & Jog, M. (2015). Simulation of particle charging and transport in corona-induced electrohydrodynamic flows. Poster #8AP.8, *American Association for Aerosol Research (AAAR) 34th annual conference*, Minneapolis, Minnesota

Liu, P., Ziemann, P. J., Kittelson, D. B., & McMurry, P. H. (1995). Generating particle beams of controlled dimensions and divergence: I. Theory of particle motion in aerodynamic lenses and nozzle expansions. *Aerosol Science and Technology*, 22(3), 293–313.

Miller, A., Frey, G., King, G., & Sunderman, C. (2010). A handheld electrostatic precipitator for sampling airborne particles and nanoparticles. *Aerosol Science and Technology*, 44(6), 417–427.

Morrow, P. E., & Mercer, T. T. (1964). A point-to-plane electrostatic precipitator for particle size sampling. *American Industrial Hygiene Association Journal*, 25(1), 8–14.

Murphy, W., & Sears, G. (1964). Production of particulate beams. *Journal of Applied Physics*, 35(6), 1986–1987.

NIOSH (2003). ELEMENTS by ICP (Hot Block/HCl/HNO3 Ashing): METHOD 7303. *NIOSH Manual of Analytical Methods*, Fourth Edition, Issue 1

Park, K., Cho, G., & Kwak, J.-H. (2009). Development of an aerosol focusing-laser induced breakdown spectroscopy (aerosol focusing-LIBS) for determination of fine and ultrafine metal aerosols. *Aerosol Science and Technology*, 43(5), 375–386.

Raynor, P. C., Leith, D., Lee, K., & Mukund, R. (2011). *Sampling and analysis using filters. Aerosol measurement: principles, techniques and applications* (3rd edition) Hoboken, NJ: John Wiley Sons, Inc..

Robinson, M. (1961). Movement of air in the electric wind of the corona discharge. *Transactions of the American Institute of Electrical Engineers, Part I: Communication and Electronics*, 80(2), 143–150.
Sioutas, C., Kim, S., & Chang, M. (1999). Development and evaluation of a prototype ultrafine particle concentrator. *Journal of Aerosol Science*, 30(8), 1001–1017. http://dx.doi.org/10.1016/S0021-8502(98)00769-1.
Sioutas, C., Koutrakis, P., & Burton, R. M. (1995). A technique to expose animals to concentrated fine ambient aerosols. *Environmental Health Perspectives*, 103(2), 172.
Spurny, K. R. (1999). *Analytical chemistry of aerosols: Science and technology* LLC, Boca Raton, FL: CRC Press.
Su, Y., Sipin, M. F., Furutani, H., & Prather, K. A. (2004). Development and characterization of an aerosol time-of-flight mass spectrometer with increased detection efficiency. *Analytical Chemistry*, 76(3), 712–719. http://dx.doi.org/10.1021/ac034797z.
Wang, X., & McMurry, P. H. (2006). A design tool for aerodynamic lens systems. *Aerosol Science and Technology*, 40(5), 320–334.
Wang, X., & McMurry, P. H. (2006). Instruction manual for the aerodynamic lens calculator. *Aerosol Science and Technology*, 40(5), 1–10.
Wu, J., Cooper, D., & Miller, R. (1989). Virtual impactor aerosol concentrator for cleanroom monitoring. *The Journal of Environmental Sciences*, 32(4), 52–56.
Yabe, A., Mori, Y., & Hijikata, K. (1978). EHD study of the corona wind between wire and plate electrodes. *AIAA Journal*, 16(4), 340–345.
Zavvos, K. (2016). *Collection and pre-concentration of aerosol for optical spectroscopies (Master thesis)* Cincinnati, OH: University of Cincinnati.
Zheng, L., Kulkarni, P., Birch, M. E., Deye, G., & Dionysiou, D. D. (2016). Near real-time measurement of carbonaceous aerosol using microplasma spectroscopy: Application to measurement of carbon nanomaterials. *Aerosol Science and Technology*, 50(11), 1155–1166. http://dx.doi.org/10.1080/02786826.2016.1224804.
Ziemann, P. J., Liu, P., Rao, N. P., Kittelson, D. B., & McMurry, P. H. (1995). Particle beam mass spectrometry of submicron particles charged to saturation in an electron beam. *Journal of Aerosol Science*, 26(5), 745–756. http://dx.doi.org/10.1016/0021-8502(95)00009-2.